High-Speed Flight of Quadrotor despite Loss of Single Rotor

Sihao Sun[1], Leon Sijbers[2], Xuerui Wang [3] and Coen de Visser[4]

Abstract— In order to achieve high-speed flight of a damaged quadrotor with complete loss of a single rotor, a multi-loop hybrid nonlinear controller is designed. By fully making use of sensor measurements, the model dependency of this control method is reduced, which is conducive to handling disturbance from unknown aerodynamic effects. This controller is tested on a quadrotor vehicle with one rotor completely removed in the high-speed condition. Free flights are performed in the Open Jet Facility (OJF), a large-scale wind tunnel. Over 9 m/s flight speed is reached for the damaged quadrotor in these tests. In addition, several high-speed spin-induced aerodynamic effects are discovered and analyzed.

I. INTRODUCTION

Multi-rotor aerial robots have the potential to be widely used in outdoor environments such as package delivery, construction monitoring, fire protection, etc. In these circumstances, vehicles usually operate in high-speed conditions where aerodynamic effects become apparent. On the other hand, owing to their task importance and safety regards, there are large demands on their ability to tolerate structural and sensor faults during the mission. To improve their resilience under both fault cases and high-speed flight conditions is a central concern for future applications.

Among these multi-rotor drones, the quadrotor excels in its structural simplicity and has been found to be more energy efficient as a delivery tool [1]. However, without actuator redundancy, this kind of vehicle suffers most from actuator failures.

Several literature sources have proposed fault-tolerant controllers in terms of actuator failures for a quadrotor. Most researchers discussed the problem with partial actuator failure in the scheme of robust control or adaptive control by regarding failures as model uncertainties [2]-[5].

Cases in which rotors are entirely missing have been discussed as well. Lanzon et al. revealed that the damaged quadrotor can be stabilized after giving up yaw control and spins around a certain axis [6]. Lippiello et al. used a strategy that transformed a damaged quadrotor into a bi-rotor after which the backstepping and PID controllers were applied [7], [8]. Lu and van Kampen proposed a three loop controller

[1]Sihao Sun is with Faculty of Aerospace Engineering, Delft University of Technology, 2629 HS Delft, The Netherlands s.sun-4@tudelft.nl
[2]Leon Sijbers is with Faculty of Aerospace Engineering, Delft University of Technology, 2629 HS Delft, The Netherlands lmcsijbers@gmail.com
[3]Xuerui Wang is with Faculty of Aerospace Engineering, Delft University of Technology, 2629 HS Delft, The Netherlands x.wang-6@tudelft.nl
[4]Coen de Visser is with Faculty of Aerospace Engineering, Delft University of Technology, 2629 HS Delft, The Netherlands c.c.devisser@tudelft.nl

Fig. 1. Figure of Open Jet Facility and the spinning quadrotor during flight.

using nonlinear control methods in conjunction with an active diagnose module [9]. Above algorithms were only validated in simulations. Mueller and D'Andrea came up with a relaxed hovering solution about which the quadrotor can be stabilized using a linear control method [10], [11], such as Linear Quadratic Regulator (LQR). This control scheme has been validated in real flight tests.

Above controllers were tested in the simulation environment or low-speed flight conditions. However, critical faults such as complete loss of efficiency in an actuator could occur while the quadrotor is cruising at high speeds at which aerodynamic effects are non-negligible. Fault-tolerant control of a severely damaged quadrotor in these circumstances has not been researched to the best of our knowledge.

The main contribution of this research is revealing the possibility of continuing high-speed cruising flight instead of a forced landing of a quadrotor of which one actuator has completely failed. A 3-loop nonlinear controller, which was initially proposed in [9], is improved in this research to achieve high-speed flight in the wind tunnel. The main feature of this cascaded controller is the usage of Incremental Nonlinear Dynamic Inversion (INDI) control in the inner loop, of which robustness to external disturbances and model uncertainties has been verified both theoretically [12] and practically [13], [14]. By virtue of the reduced model dependency of this sensor-based nonlinear controller, no model based relaxed equilibrium solutions [10] are needed and the designing process can be simplified.

Fast forward flight tests with speeds of over 9 m/s (approximately 50% of the nominal quadrotor maximum speed) have been achieved in the wind tunnel as Fig. 1 shows. For the first time, this has allowed systematic flight test experiments in regions of the flight envelope that have not been reachable using existing controllers. This, in turn, has led to the discovery of new high-speed spin-induced aerodynamics effects that when harnessed correctly could further improve the performance of a damaged quadrotor.
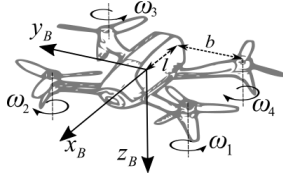
Fig. 2.   Body-fixed frame definition and graphic of Parrot Bebop2.

This paper is organized as follows: Section II introduces the dynamic model of quadrotors. Section III provides the procedure of controller design. Section IV validates the controller in a low-speed flight. High-speed flight test and analyses of aerodynamic effects are given in Section V.

II. MODEL DESCRIPTION

The inertial frame, denoted by $\mathcal{F}_I$, is defined as the reference coordinate system fixed to the ground. x_I, y_I point along and perpendicular to the wind flow respectively; z_I points to the ground. The tested quadrotor in this research is Parrot Bebop2 shown in Fig. 2. The body frame is defined fixed to the quadrotor with x_B pointing forward, y_B pointing right and z_B is the opposite of the thrust vector. For notational simplicity, the superscript 'B'and 'I' indicate the coordinate system on which the vector is projected; the subscripts 'x', 'y' and 'z' indicate the components of a 3 dimensional vector.

As shown in Fig. 2, ω_{1-4} denote rotor speeds with respect to $\mathcal{F}_B$; b and l are geometric parameters.

The equations of motion of a quadrotor based on six-dimensional rigid body dynamics is given as [15]

$$\dot{\boldsymbol{\xi}} = \boldsymbol{v} \tag{1}$$

$$m\dot{\boldsymbol{v}} = m\boldsymbol{g} + \boldsymbol{L_{IB}}\boldsymbol{F} \tag{2}$$

$$\dot{\boldsymbol{L}}_{IB} = \boldsymbol{L_{IB}}\tilde{\boldsymbol{\Omega}} \tag{3}$$

$$\boldsymbol{I_v}\dot{\boldsymbol{\Omega}} = -\tilde{\boldsymbol{\Omega}}\boldsymbol{I_v}\boldsymbol{\Omega} + \boldsymbol{M} \tag{4}$$

where $\boldsymbol{\xi}$, $\boldsymbol{v}$ indicate position and velocity respectively. $\boldsymbol{\Omega} = [p \quad q \quad r]^T$ represents the angular rate of quadrotor. The tilde superscript indicates the cross product (i.e. $\tilde{\boldsymbol{\Omega}}\boldsymbol{I_v} = \boldsymbol{\Omega} \times \boldsymbol{I_v}$). m and $\boldsymbol{I_v}$ denote mass and inertia of the vehicle. $\boldsymbol{L_{IB}}$ is the rotation matrix from $\mathcal{F}_B$ to $\mathcal{F}_I$. $\boldsymbol{g}$ is the gravity vector. $\boldsymbol{F}$ and $\boldsymbol{M}$ represent the resultant force and moment acting on the quadrotor, including the control force and moment generated by rotors.

Without loss of generality, we assume the left back rotor (ω_4) is removed and define the control input $\boldsymbol{u}$ as

$$\boldsymbol{u} = [\omega_1^2 \quad \omega_2^2 \quad \omega_3^2]^T \tag{5}$$

Therefore, a general expression of the resultant force and moment can be [16]

$$\boldsymbol{F} = \boldsymbol{F_a} + \boldsymbol{G_F}\boldsymbol{u} \tag{6}$$

$$\boldsymbol{M} = \boldsymbol{M_a} + \boldsymbol{M_g} + \boldsymbol{G_M}\boldsymbol{u} \approx \boldsymbol{M_a} + \boldsymbol{G_M}\boldsymbol{u} \tag{7}$$

where $\boldsymbol{M_g}$ is the rotor induced gyroscopic moment and is found to be negligible. $\boldsymbol{F_a}$ and $\boldsymbol{M_a}$ indicate the external

aerodynamic force and moment which are influenced by the airspeed, aerodynamic angles, angular rates, and complex interaction effects that are difficult to model accurately. In static hovering, $\boldsymbol{F_a}$ and $\boldsymbol{M_a}$ can be neglected and subsequently Eq. 6,7 become linear.

The expressions of the constant matrix $\boldsymbol{G_F}$ and $\boldsymbol{G_M}$ are

$$\boldsymbol{G_F} = \begin{bmatrix} 0 & 0 & 0 \\ 0 & 0 & 0 \\ -\kappa_0 & -\kappa_0 & -\kappa_0 \end{bmatrix}, \; \boldsymbol{G_M} = \begin{bmatrix} b\kappa_0 & -b\kappa_0 & -b\kappa_0 \\ l\kappa_0 & l\kappa_0 & -l\kappa_0 \\ \tau_0 & -\tau_0 & \tau_0 \end{bmatrix} \tag{8}$$

where κ_0 and τ_0 are force and torque coefficients respectively and can be identified using hovering flight data.

III. CONTROLLER DESIGN

A three loop controller is designed to achieve position control based on the time scale-separation assumption. Fig. 3 illustrates the controller which includes a position control loop using PID method, an attitude control loop using the primary-axis Nonlinear Dynamic Inversion (PA+NDI) and a control allocation loop using the Incremental Nonlinear Dynamic Inversion (INDI) method.

A. Position Control Loop

The outer loop is a PID controller using acceleration as virtual input

$$\boldsymbol{a_{des}} = k_p(\boldsymbol{\xi_{des}} - \boldsymbol{\xi}) + k_d(\dot{\boldsymbol{\xi}}_{des} - \boldsymbol{v}) + k_i \int (\boldsymbol{\xi_{des}} - \boldsymbol{\xi})dt, \\ (k_p, \; k_d, \; k_i > 0) \tag{9}$$

The addition of integral term will compensate the constant bias brought by aerodynamic drag.

B. Primary-Axis Attitude Control Loop

A primary-axis based attitude loop controller is designed in this section to calculate the desired angular rates p_{des} and q_{des} from $\boldsymbol{a_{des}}$.

After the removal of a single rotor, the quadrotor subsequently spins around a certain axis due to the fact that the yawing moment balance is broken [6]. The primary axis, denoted by $\boldsymbol{n}$, was introduced in [11] and defined as a unit vector about which the damaged quadrotor rotates and points at the average thrust direction in the relaxed hover solution [10]. This vector is fixed to the body frame $\mathcal{F}_B$ and can be chosen arbitrarily. If $\boldsymbol{n}$ is designed to be aligned with the instant thrust direction ($n_x^B = n_y^B = 0$) as shown in Fig. 4a, the drone spins without wobbling. An alternative way is letting $n_x^B, n_y^B > 0$ which is more energy efficient for the drone with the left back rotor removed [11], and the drone wobbles consequently as Fig. 4b shows. In addition, the following constraint should be imposed
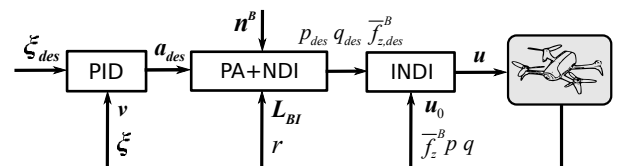

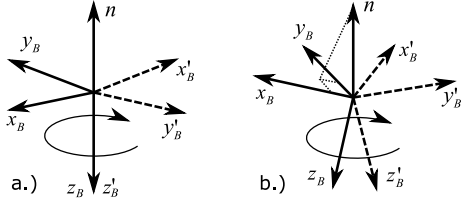Fig. 3.   Control structure of the three-loop nonlinear controller.

Fig. 4. a.) $\boldsymbol{n}$ is aligned with the instant thrust direction ($\boldsymbol{n}^B = [0\ 0\ -1]^T$). b.) $\boldsymbol{n}$ is not parallel with the instant thrust direction and the drone wobbles consequently ($\boldsymbol{n}^B \neq [0\ 0\ -1]^T$).

$$-n_z^B \geq m||\boldsymbol{g}||/T_{max} \tag{10}$$

where T_{max} denotes the available total thrust.

The task of the attitude controller is to align the direction of the primary axis $\boldsymbol{n}$ with the desired acceleration $\boldsymbol{a}_{des}$. To this end, a normalized vector pointing at a desired specific force direction is defined as $\boldsymbol{n}_{des}$ and is calculated by

$$\boldsymbol{n}_{des} = \frac{\boldsymbol{a}_{des} - \boldsymbol{g}}{||\boldsymbol{a}_{des} - \boldsymbol{g}||} \tag{11}$$

The expression of $\boldsymbol{n}_{des}$ in $\mathcal{F}_I$ is denoted by $\boldsymbol{n}_{des}^I$ and similarly, superscript B indicates the vector expressed in $\mathcal{F}_B$. The main idea of this attitude control loop is to let $\boldsymbol{n}_{des}^B$ track $\boldsymbol{n}^B$ by manipulating quadrotor angular rates. A nonlinear dynamic inversion (NDI) method is used to achieve this tracking, by taking the derivative of $\boldsymbol{n}_{des}^B$, we have

$$
\begin{aligned}
\dot{\boldsymbol{n}}_{des}^B &= d(\boldsymbol{L}_{BI}\boldsymbol{n}_{des}^I)/dt \\
&= \dot{\boldsymbol{L}}_{BI}\boldsymbol{n}_{des}^I + \boldsymbol{L}_{BI}\dot{\boldsymbol{n}}_{des}^I \\
&= -\tilde{\boldsymbol{\Omega}}\boldsymbol{n}_{des}^B + \boldsymbol{L}_{BI}\dot{\boldsymbol{n}}_{des}^I \\
&= \tilde{\boldsymbol{n}}_{des}^B\boldsymbol{\Omega} + \boldsymbol{L}_{BI}\dot{\boldsymbol{n}}_{des}^I
\end{aligned} \tag{12}
$$

For notational simplicity, we define

$$\boldsymbol{n}_{des}^B = [h_1\ \ h_2\ \ h_3]^T \tag{13}$$

thus Eq. 12 can be expanded as

$$
\begin{bmatrix} \dot{h_1} \\ \dot{h_2} \\ \dot{h_3} \end{bmatrix} = \begin{bmatrix} 0 & -h_3 & h_2 \\ h_3 & 0 & -h_1 \\ -h_2 & h_1 & 0 \end{bmatrix} \begin{bmatrix} p \\ q \\ r \end{bmatrix} + \boldsymbol{L}_{BI}\dot{\boldsymbol{n}}_{des}^I \tag{14}
$$

Since the matrix $\tilde{\boldsymbol{n}}_{des}^B$ is singular and cannot be inverted, a subsystem $[h_1\ \ h_2]^T$ is to be stabilized. This is similar to the process introduced in [9], whereas the $\boldsymbol{n}_{des}^B = [h_1\ \ h_2\ \ h_3]^T$ is defined as the state and the primary axis $\boldsymbol{n}^B = [n_x^B\ \ n_y^B\ \ n_z^B]^T$ is defined as reference in our method. This distinction is important since the original method shows inability to stabilize the drone due to measurement noise and model uncertainty in the experiment. Note that $\sqrt{h_1^2 + h_2^2 + h_3^2} = 1$, therefore an accurate tracking of h_1 and h_2 to their reference value (the first two components of $\boldsymbol{n}^B$) will also guarantee the tracking of h_3. Denote $\hat{\boldsymbol{n}}_{des}^I$ as a vector composed of the x and y component of $\boldsymbol{L}_{BI}\dot{\boldsymbol{n}}_{des}^I$

and a subspace system is separated from Eq. 14 yielding

$$
\begin{bmatrix} \dot{h_1} \\ \dot{h_2} \end{bmatrix} = \begin{bmatrix} 0 & -h_3 \\ h_3 & 0 \end{bmatrix} \begin{bmatrix} p \\ q \end{bmatrix} + \begin{bmatrix} h_2 \\ -h_1 \end{bmatrix} r + \hat{\boldsymbol{n}}_{des}^I \tag{15}
$$

Now, replace the left-hand side of Eq. 15 by the virtual input $\boldsymbol{\nu}_{out}$, we have

$$
\begin{bmatrix} p_{des} \\ q_{des} \end{bmatrix} = \begin{bmatrix} 0 & 1/h_3 \\ -1/h_3 & 0 \end{bmatrix} \left(\boldsymbol{\nu}_{out} - \begin{bmatrix} h_2 \\ -h_1 \end{bmatrix} r - \hat{\boldsymbol{n}}_{des}^I \right) \tag{16}
$$

where

$$
\boldsymbol{\nu}_{out} = \begin{bmatrix} \dot{n}_x^B + k_x(n_x^B - h_1) \\ \dot{n}_y^B + k_y(n_y^B - h_2) \end{bmatrix} \qquad (k_x, k_y > 0) \tag{17}
$$

Note that $\dot{n}_x^B$ and $\dot{n}_y^B$ are zero since the primary axis is fixed to the vehicle.

In the attitude controller Eq. 16, only pitch and roll rate are assigned (p_{des} and q_{des}). The yaw rate r is measured onboard and used as a state information for the controller. This property is essential for achieving high speed flight because the yaw rate is found to vary with the flight speed and the heading angle as Section V shows. It is worth noting that a nominal drone with zero or small yaw rate may also use this method in conjunction with an individual yaw controller.

The magnitude of the desired acceleration should be determined by thrust which is computed using the same method introduced in [10].

$$n_z^B \bar{f}_{z,des}^B \boldsymbol{n}_{des} = \boldsymbol{L}_{BI}(\boldsymbol{a}_{des} - \boldsymbol{g}) \tag{18}$$

where $\bar{f}_{z,des}^B = -T_{des}/m$ indicates the desire specific force on the z_B.

C. Control Allocation Loop

The control allocation loop converts p_{des}, q_{des} and $\bar{f}_{z,des}^B$ to the rotor speed commands. With the existence of both fast spinning and high speed inflow, the aerodynamic effects significantly influence the rotational dynamics of the quadrotor [16]. Since the moment from the aerodynamics (the abovementioned $\boldsymbol{M}_a$) is difficult to model, a model based control allocation method may be impractical. On the other hand, the Incremental Nonlinear Dynamic Inversion (INDI) method is applicable to this problem [12], [13]. Consider a general system $\dot{\boldsymbol{x}} = \boldsymbol{f}(\boldsymbol{x}, \boldsymbol{u})$ with the output $\boldsymbol{y} = \boldsymbol{C}\boldsymbol{x}$. Then the dynamics of the output $\boldsymbol{y}$ can be expressed in an incremental form as

$$
\begin{aligned}
\dot{\boldsymbol{y}} &= \boldsymbol{C}\dot{\boldsymbol{x}} = \boldsymbol{C}\boldsymbol{f}(\boldsymbol{x}, \boldsymbol{u}) \\
&= \boldsymbol{C}\dot{\boldsymbol{x}}_0 + \boldsymbol{C}\frac{\partial \boldsymbol{f}}{\partial \boldsymbol{x}}\big|_0 \Delta \boldsymbol{x} + \boldsymbol{C}\frac{\partial \boldsymbol{f}}{\partial \boldsymbol{u}}\big|_0 \Delta \boldsymbol{u} + \boldsymbol{C}\mathcal{O}(\Delta \boldsymbol{x}^2, \Delta \boldsymbol{u}^2) \\
&= \dot{\boldsymbol{y}}_0 + \hat{\boldsymbol{G}}\Delta \boldsymbol{u} + \boldsymbol{\epsilon}
\end{aligned} \tag{19}
$$

where $\Delta \boldsymbol{x} = \boldsymbol{x} - \boldsymbol{x}_0$, $\Delta \boldsymbol{x} = \boldsymbol{u} - \boldsymbol{u}_0$ and $\boldsymbol{y}_0$, $\boldsymbol{u}_0$ stand for the measured output and input at the last sample when system states are $\boldsymbol{x}_0$. The matrix $\hat{\boldsymbol{G}}$ is an estimation of the control effectiveness matrix $\boldsymbol{C}\frac{\partial \boldsymbol{f}}{\partial \boldsymbol{u}}\big|_0$. The residual, $\boldsymbol{\epsilon}$, includes three elements: the $\boldsymbol{C}(\frac{\partial \boldsymbol{f}}{\partial \boldsymbol{u}}\big|_0 - \hat{\boldsymbol{G}})\Delta \boldsymbol{u}$ term which comes from the estimation error of the control effectiveness matrix,

the $C\frac{\partial f}{\partial x}\big|_0 \Delta x$ term and the Taylor expansion remainder $C\mathcal{O}(\Delta x^2, \Delta u^2)$.

For a Bebop2 quadrotor with the left back rotor removed, define the system output as $\boldsymbol{y} = [p \quad q \quad \int \bar{f}_z^B dt]^T$, where $\bar{f}_z^B$ denotes the specific force on z_B direction which can be measured by the accelerometer. The incremental form of $\dot{\boldsymbol{y}}$ is

$$
\begin{aligned}
\dot{\boldsymbol{y}} &= \dot{\boldsymbol{y}}_0 + \hat{\boldsymbol{G}}\Delta\boldsymbol{u} + \boldsymbol{\epsilon} = \begin{bmatrix} \dot{p}_0 & \dot{q}_0 & \bar{f}_{z,0}^B \end{bmatrix}^T \\
&+ \begin{bmatrix} b\kappa_0/I_{vx} & -b\kappa_0/I_{vx} & -b\kappa_0/I_{vx} \\ l\kappa_0/I_{vy} & l\kappa_0/I_{vy} & -l\kappa_0/I_{vy} \\ -\kappa_0/m & -\kappa_0/m & -\kappa_0/m \end{bmatrix} (\boldsymbol{u} - \boldsymbol{u}_0) + \boldsymbol{\epsilon}
\end{aligned}
\tag{20}
$$

where $\boldsymbol{u}$ is defined in the Eq. 5; p_0, q_0 and $\bar{f}_{z,0}^B$ are the last measured angular rate and specific force. The $\hat{\boldsymbol{G}}$ matrix is estimated using Eq. 8 and assuming $I_{vxy} = 0$. Recall Eq. 4-7, the major effects of the coupling term $-\tilde{\boldsymbol{\Omega}}\boldsymbol{I}_v\boldsymbol{\Omega}$, the aerodynamic force $\boldsymbol{F}_a$ and moment $\boldsymbol{M}_a$ are included in the $\dot{\boldsymbol{y}}_0$, which can be obtained from sensor measurements instead of accurate models. By virtue of the high sampling frequency of the sensors (512 Hz for the Bebop2), the influence of $\boldsymbol{\epsilon}$ becomes negligible, thus can be omitted [12].

Particularly, $\dot{\boldsymbol{y}}_0$ is obtained by taking derivative of the gyroscope and accelerometer measurements. The considerable noise of these measurements is reduced by a first-order low-pass filter [13]. To compensate the lag introduced by the filter, the input measurement $\boldsymbol{u}_0$ needs to be filtered with the same cut-off frequency to maintain synchronization between input increment and measured rotation accelerations. This process introduces the filtered measurements $\dot{\boldsymbol{y}}_f$ and $\boldsymbol{u}_f$ to replace $\dot{\boldsymbol{y}}_0$ and $\boldsymbol{u}_0$ in the Eq. 20. Finally, the desired rotor speed command can be obtained by

$$
\boldsymbol{u} = \hat{\boldsymbol{G}}^{-1}(\boldsymbol{\nu}_{in} - \dot{\boldsymbol{y}}_f) + \boldsymbol{u}_f
\tag{21}
$$

where

$$
\boldsymbol{\nu}_{in} = \begin{bmatrix} \dot{p}_{des} + k_1(p_{des} - p) \\ \dot{q}_{des} + k_2(q_{des} - q) \\ \bar{f}_{z,des}^B + k_3\int(\bar{f}_{z,des}^B - \bar{f}_z^B)dt \end{bmatrix} \quad (k_1, k_2, k_3 > 0)
\tag{22}
$$

To satisfy the time-scale separation assumption, the gains in the inner loop should be larger than the outer loop gains yielding

$$
\min\{k_1, k_2, k_3\} > \max\{k_x, k_y\}
\tag{23}
$$

IV. VALIDATION

In order to validate the above nonlinear controller first without significant aerodynamic effects, low-speed flight tests are carried out in the Cyberzoo, an indoor flight test field operated by the Delft University of Technology. The inertia and geometry parameters of the tested quadrotor, Parrot Bebop2, are listed in Table I. To alleviate the effects of actuator saturation, the quadrotor is lightened by removing the camera and a lighter weight battery is used. The processor is a Parrot P7 dual-core CPU Cortex 9. The onboard sensor is MPU6050 for accelerometers and gyroscope with 512Hz sampling rate. Other hardware information about this type of drone can be found in [17]. An open source autopilot,

Paparazzi [18], is modified to run the algorithm. An external motion capturing system (Optitrack) is operated at 120Hz and provides the position measurements of 6 reflecting markers fixed to the drone. The position of the center of gravity, velocity and attitude are then derived from these measurements and are transmitted to the on-board controller via WiFi.

In the flight tests, the drone was controlled to track a certain trajectory as shown in Fig. 5a. As compared to the linear controller adopted in [6], no prior-calculated solutions are required. To illustrate the advantage of the nonlinear controller, the primary axis was set to change at 7s from $\boldsymbol{n}^B = [0.1 \quad 0.1 \quad -1.00]^T$ to $\boldsymbol{n}^B = [0.2 \quad 0.2 \quad -0.96]^T$ without any prior calculation and using the same set of gains. As a consequence, the reference value of h_1 and h_2 changed from 0.1 to 0.2 which can be clearly seen in the Fig. 5b. The p_{des}, q_{des} calculated from Eq. 16 and the measured p and q are presented in Fig. 5c. The slight errors of tracking on p and q can be observed and subsequently lead to the tracking errors of h_1 and h_2. As a consequence, the orientation of the primary axis $\boldsymbol{n}^I$ oscillated about the $\boldsymbol{n}_{des}^I$ as Fig. 6 shows. However, the average thrust can still align with the $\boldsymbol{n}_{des}^I$ and subsequently guarantee position control. The average thrust direction is calculated by implementing a forward-backward low-pass filter on the primary axis $\boldsymbol{n}^I$ with 2Hz

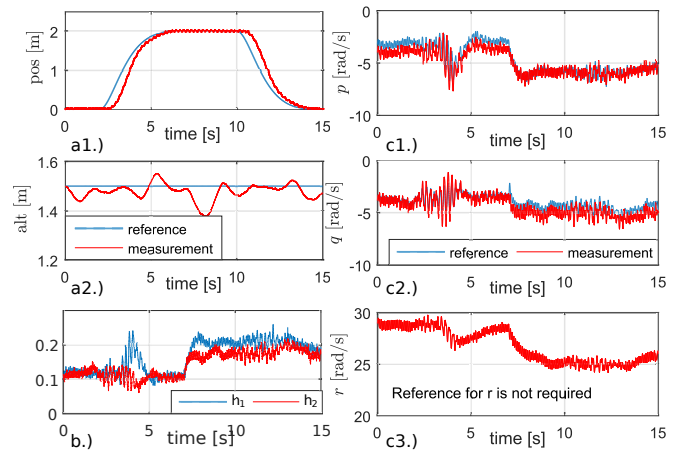Fig. 5. a.) Reference trajectory and the measured position. b.) Time series of h_1, h_2. The reference value of them changed from 0.1 to 0.2 at t=7s. c.) Reference value of pitch rate, roll rate and measurement value of angular rates. The reference and real values changed at t=7s when primary axis is changed.
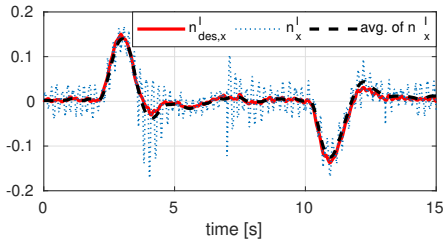
Fig. 6. Time series of the desired primary axis direction $n_{x,des}^I$, the real direction of primary axis n_x^I, and the average value of n_x^I. Although the primary axis oscillates around $n_{x,des}^I$, its average value is perfectly aligned with it, which ensures desirable position tracking performance.
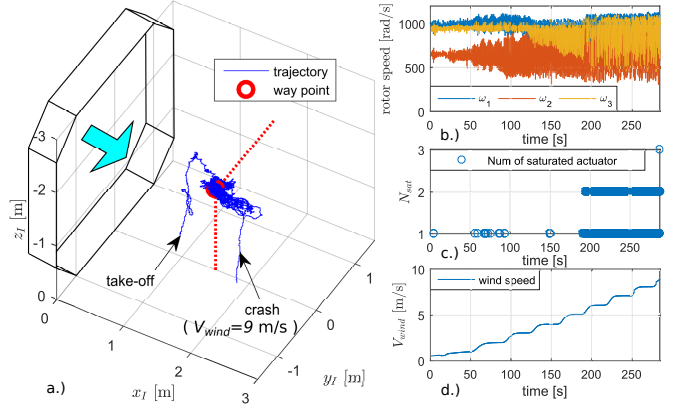

Fig. 7. a.) 3D trajectory in a single wind tunnel flight test and the way point to be tracked. b.)Time series of rotor speed. c.) The number of saturated actuator. d.) Time series of the wind speed. In this flight, the rotor #4 was removed. The drone crashed at around 9 m/s when all three rotors reached their speed limits.

cut-off frequency.

The measured yaw rate r is also given in Fig. 5c. A positive yaw rate stands for a clockwise spinning direction. It is obvious that the yaw rate reduced after the primary axis is changed since a more tilted primary axis leads to a larger wobbling angle and a smaller spinning rate [11].

V. WIND TUNNEL FLIGHT TEST

To validate the controller in the high-speed condition and reveal the aerodynamic effects acting on the spinning quadrotor, flight tests have been carried out in the Open Jet Facility (OJF), a large scale wind tunnel with a 3 m by 3 m aperture as Fig. 1 shows. The external motion capturing system is also mounted in the OJF, which contains 12 cameras providing an area of 2 m × 2 m × 3 m for consistent tracking of the drone. The other experimental settings are same as those introduced in Section IV. The damaged quadrotor is controlled to track a way point 1.5 m away from the wind tunnel nozzle. The wind speed is initialized from 0 m/s and increased in steps of 1 m/s until the drone crashes. Both clockwise and counterclockwise rotating rotors are disabled leading to different spinning directions of the quadrotor. As a result, the drone is able to maintain stable flight until the wind speed reaches over 9 m/s, which is approximately 50% of the maximum flight speed in nominal case.

Fig. 7a demonstrates the 3-D trajectory of a single flight the left back rotor removed and $\mathbf{n^B} = [0.2\ 0.2\ -0.96]^T$. Fig. 7d shows the wind speed from the time when the drone starts to be stabilized at the way point until it crashes due to the violent aerodynamic effects. Fig. 7b presents the time history of the rotor speeds of which the level of fluctuation grows with the wind speed, which can be interpreted as the effect of aerodynamics. Saturation of the actuator occurs and its severity increased with higher wind speeds as is shown in Fig. 7c. When the speed is higher than 5 m/s, two propellers reached saturation. The drone finally crashed when three remaining actuators reached their limit. Therefore, the actuator saturation is suspected to be the main reason for the loss of control.

A. Effect of Aerodynamic Moment

In order to analyze the aerodynamic effects, two variables are introduced. The airspeed, denoted by V, indicates the

relative speed between the drone and the coming flow and can be calculate by

$$V = ||\boldsymbol{v} - \boldsymbol{V}_{wind}|| \tag{24}$$

where $\boldsymbol{V}_{wind}$ represents the vector of wind velocity. The heading angle of the drone, denoted by ψ, is considered to be pointing towards the nozzle (against the wind) when $\psi = 0$.

From the high-speed flight data, the effect of the aerodynamic moment $\boldsymbol{M_a}$ is found to be considerable. This leads to a significant distinction from the hovering conditions. To estimate this aerodynamic moment, the resultant moment $\boldsymbol{M}$ is calculated by Eq. 4 using the method introduced in [16]. Subsequently, $\boldsymbol{M_a}$ can be calculated from Eq. 7.

It is indicated that the aerodynamic induced rolling and pitching moment denoted by $M_{a,x}$ and $M_{a,y}$ are highly correlated to the heading angle ψ. Fig. 8b shows the value of $M_{a,x}$ and $M_{a,y}$ at different heading angles from the data including 20 rotations at airspeed of 4 m/s. The magnitude of these moments are considerable with respect to the size and inertia of Bebop2 quadrotor. To stabilize the quadrotor under these heading angle related moments, the rotor speeds are found to vary with the heading angle as presented in Fig. 8a accounting for the vast fluctuation of the rotor speeds in the high-speed condition as shown in Fig. 7b. By contrast, in the hovering condition without significant aerodynamic effects, the rotor speeds are supposed to keep constant in one rotation.

As is shown in Fig. 8c, the rotor speed fluctuation also lead to the variation of the yaw rate. For ex, a yaw rate reduction occurs at the airspeed of 4 m/s and 6 m/s from $\psi = 110°$ to $\psi = 200°$ while ω_2 is increasing and ω_3 is decreasing. The airspeed also influences the mean value of the yaw rate. As the wind speed increased from 0 m/s to 4 m/s, a dramatic drop-off appears which can be caused by the mis-tracking of the primary-axis due to the aerodynamic moment. The primary axis is not perfectly tracked in these conditions, nev-
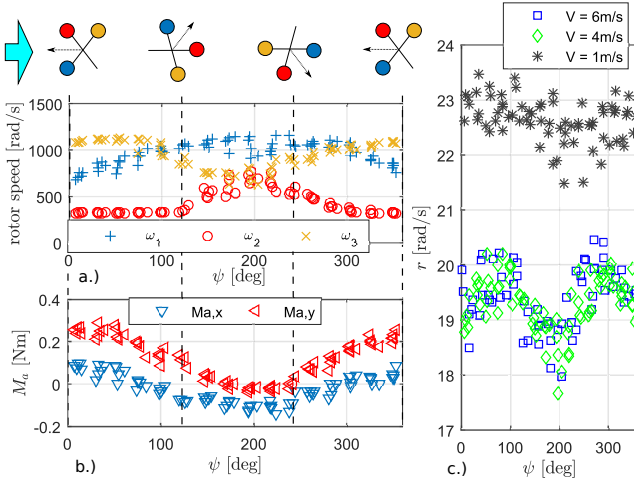
Fig. 8. a.) Rotor speeds vary significantly with the heading angle, plotted data are with $V = 4$ m/s containing 20 revolutions. b.) Aerodynamic rolling moment $M_{a,x}$ and $M_{a,y}$ acting on the quadrotor. c.)Comparison of the yaw rate in different flight speeds. Yaw rate varies with the heading angle when $V > 0$ m/s.
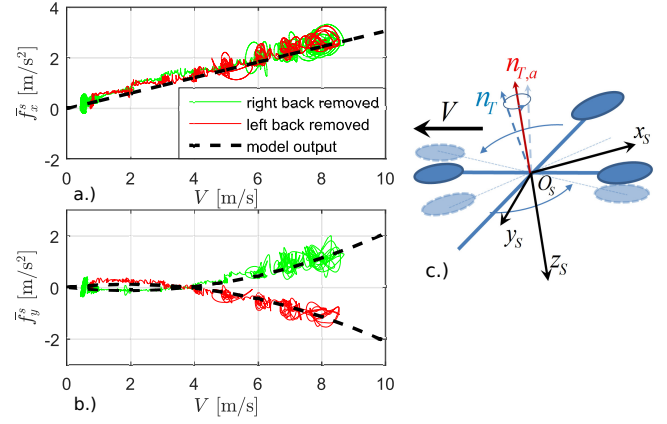

Fig. 9. a.) Specific force projecting on the stability coordinate system. The drag force $\bar{f}_x^s$ is linear with the flight speed. b.) The lateral-force $\bar{f}_y^s$ is positive related to the flight speed and its direction varies with the quadrotor spinning direction. Model identified from the data with the right-back rotor removed are compared in the black dash line. c.) The definition of the stabilization frame. $\boldsymbol{n}_T$ indicates the instant thrust direction and $\boldsymbol{n}_{T,a}$ indicates the average thrust direction.

ertheless, the average thrust can still align with the desired acceleration direction to maintain the position tracking, as was analyzed in Section IV.

B. Necessity of Applying Robust Nonlinear Controller

According to the assumption and flight validation results presented in [11], the resultant moment acting on the quadrotor in the hovering condition can be expressed as

$$\boldsymbol{M} = \begin{bmatrix} 0 & 0 & -\gamma \end{bmatrix}^T r + \boldsymbol{G_M}\boldsymbol{u} \qquad (25)$$

where $\gamma > 0$ is the yaw damping coefficient. It is clear that near hovering conditions, the resultant moment is linear to the states and control inputs. Thus knowing the information of the $\boldsymbol{G_M}$ matrix and the yaw damping coefficient γ, a linear controller such as the Linear Quadratic Regulator (LQR) can be well designed[10], [11].

On the other hand, in the high-speed flight conditions, the resultant moment $\boldsymbol{M}$ is highly nonlinear with respect to the speed, angular rate, and heading angle on the basis of the flight data and literature about rotor aerodynamic characteristics[19]-[21], yielding

$$\boldsymbol{M} = \boldsymbol{M_a}(V, \psi, \boldsymbol{\Omega}) + \boldsymbol{G_M}\boldsymbol{u} \qquad (26)$$

For this reason, designing a satisfying gain-scheduling controller requires an accurate model of $\boldsymbol{M_a}(V, \psi, \boldsymbol{\Omega})$, which is difficult to obtain. Even if true, a large number of set points and gain (matrices) need to be computed and tuned at different V, ψ and $\boldsymbol{\Omega}$, which is possible but impractical.

In comparison, the INDI controller has two significant advantages. First, the aerodynamic model is not required since the effects of $\boldsymbol{M_a}$ are included in the $\dot{\boldsymbol{y}}_0$ term in Eq. 19. Secondly, only a small number of gains (k_x, k_y, k_1, k_2, k_3) need to be tuned. We believe that other nonlinear/robust controllers are also applicable, to some extend, by knowing the model of $\boldsymbol{M_a}$ or regarding it as an external disturbance.

C. Aerodynamic force model

The simplified aerodynamic force model can be identified from the flight data for further analyzing the performance of the damaged quadrotor, such as the maximum flight speed and range, etc.

Since the quadrotor spins at a high rate (approximately 20 rad/s), we introduce the stabilization frame, denoted by $\mathcal{F}_S$, to describe the forces acting on the entire spinner. As Fig. 9c illustrates, z_S points against the average direction of the thrust vector; x_S lies in the plane formed by the gravity and the airspeed and points against the airspeed direction; y_S is perpendicular to the $O_S x_S z_S$ plane and points to the left. The motion capturing system is used to measure the specific forces acting on the quadrotor by differentiating measured velocities. Because of the slight misalignment between the rotation center and the rigid body center interpreted by the motion capturing system, the measured velocity oscillates with the spinning frequency of the quadrotor. A low-pass filter with cut-off frequency lower than the spinning frequency is applied to the measured velocity to obtain $\boldsymbol{v_f}$ and the estimated specific force can be calculated by

$$\bar{\boldsymbol{f}} = d\boldsymbol{v_f}/dt - \boldsymbol{g} \qquad (27)$$

Two sets of flight data are plotted in Fig. 9 showing the airspeed versus specific forces which are expressed in $\mathcal{F}_S$. The index of the removed rotor is the only difference between these two flights, where the case without right back rotor is plotted in green and left back in red. As a consequence, the damaged quadrotor losing its left back rotor spins clockwise (from the top view) and vise versa.

Fig. 9a shows the specific force along x_S, i.e. $\bar{f}_x^B$, which can be interpreted as the drag. A linear relationship between V and $\bar{f}_x^B$ can be clearly seen. Note that this linear relationship also holds for the nominal quadrotor [22], indicating the

spinning motion may bring high-frequency force deviation on the drone but the linear trend still holds. For two damage types with different spinning directions, the slope remains the same. Therefore, a linear model can be identified to predict the drag specific force in the form of

$$\bar{f}_x^s = C_x V \tag{28}$$

where C_x is the drag coefficient.

As Fig. 9b shows, the lateral force appears and its direction varies with the spinning direction. For anticlockwise rotation, the lateral force is slightly positive when flight speed is smaller than 3.5 m/s and then become negative as flight speed increases. On the other hand, the data from clockwise rotation shows a nearly opposite pattern. The asymmetric configuration of the spinning quadrotor under fault condition can be the major cause of this lateral force. Therefore, the lateral specific force can be modeled as

$$\bar{f}_y^s = sign(r)(C_{y,1}V + C_{y,2}V^2) \tag{29}$$

Flight data with the right back rotor removed are used for identifying the C_x, $C_{y,1}$ and $C_{y,2}$ using a Least Square estimator. The model is verified using the data with left back rotor removed as Fig. 9 shows. The drag coefficients of the tested Bebop2 quadrotor are listed in Table II.

VI. CONCLUSIONS

A 3-loop nonlinear controller is designed and tested on a quadrotor with one rotor removed. High-speed flight tests are carried out systematically in the wind tunnel. The new control scheme possesses robustness against complex aerodynamic effects brought by both fast translational and fast spinning motion of a damaged quadrotor. The research shows that quadrotors with severe actuator damage can continue high-speed missions instead of having to immediately abort.

Several high-speed spinning-induced aerodynamic effects have been discovered. Rotor speeds and the yaw rate which are constant in the hovering conditions are found to vary with the heading angle in the high-speed flight. Aerodynamic moments are observed to significantly increase the nonlinearity of the system. Aerodynamic forces, especially the lateral force induced by the spinning motion, are observed and modeled. Understanding of these effects could further help to improve the performance of a damaged quadrotor and increase its fault tolerance which is essential for a broader acceptance of multi-rotor drones by the public.

Future research will focus on further modeling these aerodynamic effects and analyze flight envelope shrinkage. In terms of controller improvement, actuator saturation effects will be considered to further increase the maximum flight speed of the damaged quadrotor.

REFERENCES

[1] J. K. Stolaroff, C. Samaras, E. R. ONeill, A. Lubers, A. S. Mitchell, and D. Ceperley, Energy use and life cycle greenhouse gas emissions of drones for commercial package delivery, Nat. Commun., vol. 9, no. 1, p. 409, 2018.

[2] L. Besnard, Y. B. Shtessel, and B. Landrum, Quadrotor vehicle control via sliding mode controller driven by sliding mode disturbance observer, J. Franklin Inst., vol. 349, no. 2, pp. 658-684, 2012.

[3] T. Li, Y. Zhang, and B. W. Gordon, Passive and active nonlinear fault-tolerant control of a quadrotor unmanned aerial vehicle based on the sliding mode control technique, Spec. Issue Artic. Proc IMechE Part I J Syst. Control Eng., vol. 227, no. 1, pp. 12-23, 2012.

[4] A. R. Merheb, H. Noura, and F. Bateman, Design of Passive Fault-Tolerant Controllers of a Quadrotor Based on Sliding Mode Theory, Int. J. Appl. Math. Comput. Sci., vol. 25, no. 3, pp. 561-576, 2015.

[5] Y. M. Zhang, A. Chamseddine, C. A. Rabbath, B. W. Gordon, C. Y. Su, S. Rakheja, C. Fulford, J. Apkarian, and P. Gosselin, Development of advanced FDD and FTC techniques with application to an unmanned quadrotor helicopter testbed, J. Franklin Inst., vol. 350, no. 9, pp. 2396-2422, 2013.

[6] A. Lanzon, A. Freddi, and S. Longhi, Flight Control of a Quadrotor Vehicle Subsequent to a Rotor Failure, J. Guid. Control. Dyn., vol. 37, no. 2, pp. 580-591, 2014.

[7] V. Lippiello, F. Ruggiero, and D. Serra, Emergency Landing for a Quadrotor in Case of a Propeller Failure : A Backstepping Approach, no. Iros, pp. 4782-4788, 2014.

[8] V. Lippiello, F. Ruggiero, and D. Serra, Emergency Landing for a Quadrotor in Case of a Propeller Failure : A PID Based Approach.

[9] P. Lu and E. van Kampen, Active fault-tolerant control for quadrotors subjected to a complete rotor failure, no. Iros, pp. 4698-4703, 2015.

[10] M. W. Mueller and R. DAndrea, Relaxed hover solutions for multicopters: Application to algorithmic redundancy and novel vehicles, Int. J. Rob. Res., p. 873-889, 2015.

[11] M. W. Mueller and R. DAndrea, Stability and control of a quadrocopter despite the complete loss of one, two, or three propellers, Proc. - IEEE Int. Conf. Robot. Autom., pp. 45-52, 2014.

[12] X. Wang, E.-J. Van Kampen, Q. P. Chu, and P. Lu, Stability Analysis for Incremental Nonlinear Dynamic Inversion Control, in 2018 AIAA Guidance, Navigation, and Control Conference, 2018, no. January, pp. 1-17.

[13] E. J. J. Smeur, Adaptive Incremental Nonlinear Dynamic Inversion for Attitude Control of Micro Aerial Vehicles, J. Guid. Control. Dyn., vol. 39, no. 3, pp. 450-461, 2016.

[14] E. J. J. Smeur, Q. Chu, and G. C. H. E. de Croon, Gust Load Alleviation with Incremental Nonlinear Dynamic Inversion, Int. Conf. Robot. Autom. ICRA 2016, 2016.

[15] R. Mahony, V. Kumar, and P. Corke, Multirotor Aerial Vehicles: Modeling, Estimation, and Control of Quadrotor, Robot. Autom. Mag. IEEE, vol. 19, no. 3, pp. 20-32, 2012.

[16] S. Sun, R. J. Schilder, and C. C. De Visser, Identification of Quadrotor Aerodynamic Model from High Speed Flight Data, AIAA Atmos. Flight Mech. Conf.,no. January, pp. 1-23, 2018.

[17] https://wiki.paparazziuav.org/wiki/Bebop

[18] https://github.com/paparazzi/paparazzi

[19] G. M. Hoffmann, H. Huang, S. L. Waslander, and C. J. Tomlin, Precision flight control for a multi-vehicle quadrotor helicopter testbed, Control Eng. Pract., vol. 19, no. 9, pp. 10231036, 2011.

[20] P. Bristeau, P. Martin, E. Salan, and N. Petit, The role of propeller aerodynamics in the model of a quadrotor UAV, 2009.

[21] W. Johnson, Helicopter theory, New York. pp. 164, 1980.

[22] R. C. Leishman, J. C. MacDonald, R. W. Beard, and T. W. McLain, Quadrotors and accelerometers: State estimation with an improved dynamic model, IEEE Control Syst., vol. 34, no. 1, pp. 28-41, 2014.